

Imaging Optical Properties of Thin-Film Coatings and Devices with High Spatial Resolution and Sensitivity Using Pump–Probe and Photon-Counting Techniques

Introduction

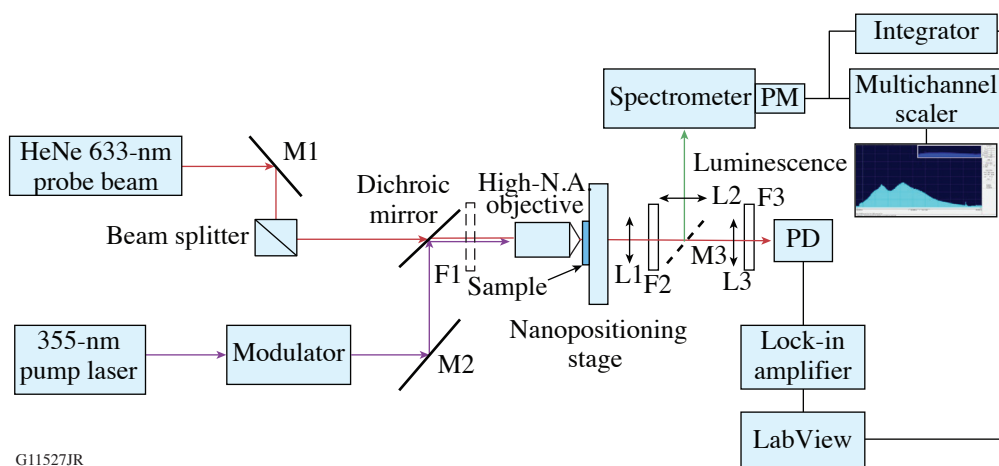
Imaging optical properties of the materials with high spatial resolution and sensitivity is an important part of the research in such areas as material science, biology, medicine, and optical computing. The most important instruments used for this purpose are a confocal microscope and a scanning near-field optical microscope (SNOM), which allows one to create sample luminescence maps with ~ 100 -nm resolution. Still, if one desires to obtain not only luminescence but also absorption data from the same location, the standard configuration of the SNOM makes such measurements impossible. In this work we describe a relatively simple setup that allows one to create absorption and luminescence maps with ~ 0.35 - μm spatial resolution. This setup uses a pump/probe-based photothermal heterodyne imaging (PHI) technique^{1,2} for absorption mapping in one arm and a spectrometer with a photon-counting detector for luminescence mapping in the other arm. The mapping is accomplished by mounting the sample on the nanopositioning stage, which permits raster scanning of the sample. High spatial resolution is achieved by using a high-numerical-aperture

(N.A.) objective to focus pump and probe laser beams on the sample into the submicrometer spot.

The Setup's Schematic and Parameters

1. Absorption Mapping

The schematic of the setup is presented in Fig. 156.8. Photothermal absorption mapping is accomplished by using a 355-nm, 40-mW continuous-wave pump laser (Genesys, Coherent) and a 632.8-nm, 10-mW HeNe probe laser. The pump-laser beam passes through an acousto-optic modulator (Brimrose), where the modulation frequency Ω is optimized in the range of 300 kHz to 400 kHz for the best signal-to-noise performance. Using a dichroic mirror, the pump beam diffracted into the first order (maximum power ~ 10 mW) and the probe beam are collinearly combined at the entrance aperture of the high N.A. objective ($40\times/0.95$ N.A. Olympus or $40\times/0.5$ N.A. Thorlabs reflective objective), focusing both beams on the sample into an overlapping submicrometer spot (see Fig. 156.9). Beam overlapping is achieved by raster scanning a 1 - μm pinhole mounted on the nanopositioning stage (Physik Instrumente) in



G11527JR

Figure 156.8

Schematic of the setup for absorption and photoluminescence mapping with submicrometer resolution. Optical elements designated by letters are as follows: L1, L2, and L3 are the lenses collecting and focusing light; M1 and M2 are beam transport mirrors; M3 is a flip mirror; F1 is a short-pass filter rejecting stray light during luminescence measurements; F2 is a long-pass filter rejecting 355-nm pump light; F3 is a narrowband, 633-nm-pass filter; and PD and PM are photodiode and photomultiplier detectors, respectively. Elements shown by broken lines (F1 and M3) are inserted only for luminescence measurements.

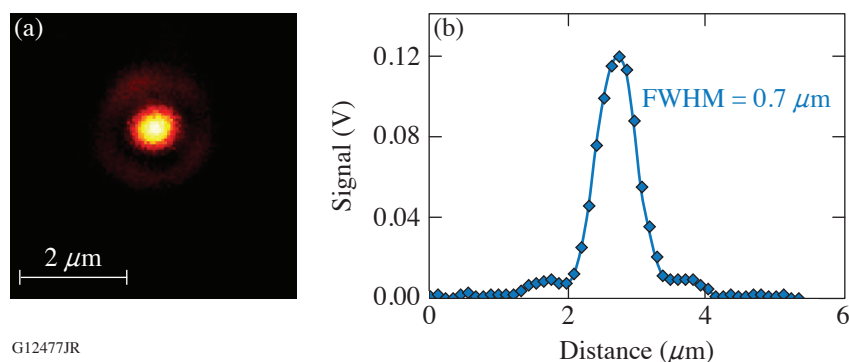


Figure 156.9

Combined focal spot of the pump and probe beams. (a) Image obtained with a 1- μm pinhole; (b) cross-sectional profile taken through the beam center. The measured 0.7- μm FWHM beam size is limited by the transfer function of the 1- μm pinhole and should be considered as an upper limit.

G12477JR

the objective focusing plane (plane normal to the beam propagation) and using angular tuning of the dichroic mirror (see Fig. 156.8). The stage has a minimum lateral step size of 10 nm, a maximum scan size of 200 μm , and a z -axis displacement of 20 μm . To achieve a best-focus spot and combine the focusing points for pump and probe beams, two beam expanders [each incorporated into the pump and probe beam path (not shown in Fig. 156.8)] are used to overfill the objective aperture and tune the beam divergence characteristics. The energy absorption from the pump beam generates heating of the sample material and modulation of the local refractive index n because of index temperature dependence $n(T)$, which results in modulated scattering of the probe laser beam. In a case when the absorber is much smaller than the pump-beam spot, heat conduction to the surrounding material causes both an increase in the scattering volume and a change in the probe-laser frequency from ω to $\omega \pm \Omega$ because of Doppler shift. In the far field, the scattered probe light interferes with much more intensive light passing without scattering, which produces light with an amplified beat intensity $I = I(\Omega)$ described by the following equation:¹

$$I(\Omega) \sim I_{\text{pump}} I_{\text{probe}} n \frac{\partial n}{\partial T} \lambda^{-2} w^{-1} F(\Omega), \quad (1)$$

where I_{pump} and I_{probe} are the pump and probe intensities; λ and w are the probe wavelength and beam waist, respectively; and $F(\Omega)$ is a function describing the signal's dependence on modulation frequency. This light, collected by the same objective (backward configuration) or additional lens (L1) in our case (forward configuration), is focused by the L3 lens onto the silicon diode detector, which produces a modulated signal further amplified by a lock-in amplifier (Stanford Research Systems SR844) and processed by LabVIEW-based data-acquisition software. The narrowband 633-nm pass filter ensures that stray light, including UV-pump light, does not reach the photodiode. The signal is mapped by raster scanning the sample mounted on the same nanopositioning stage. It should be noted here that there are other photothermal techniques, such as photothermal deflection³ and common-path interferometry,⁴ with superior to

PHI sensitivity—better than 1×10^{-6} (one part per million). Unique to the PHI technique is a combination of respectable sensitivity of ~ 40 parts per million (Ref. 5) and submicrometer spatial resolution, making it possible to detect localized absorbers as small as a few nanometers.¹ More details about the PHI technique can be found in Refs. 1 and 2.

2. Luminescence Mapping

Detection and mapping of the luminescence are accomplished by flipping the M3 mirror, which sends the light collected from the sample by the L1 lens into the spectrometer (Newport/Oriel MS260i) entrance slit. Using another lens (L2) ensures that the entrance slit is properly illuminated by matching the f number of the spectrometer's entrance mirror. An additional short-pass filter is introduced before the high-N.A. objective in order to reject any visible and near-infrared light coming from the laboratory environment. The spectrometer operates with a grating that covers a spectral range of 300 nm to 800 nm and has 17-nm/mm spectral resolution. A cooled light detector (photomultiplier H8259, Hamamatsu) is mounted on the output slit and works in a photon-counting regime. The spectra recording is accomplished by scanning the spectrometer grating and integrating detector counts for each spectral position using a multichannel scaler (ORTEC EASY-MCS), whose channels are calibrated in the wavelength units. The typical count accumulation time for each channel is about 1 s, and the total spectrum recording time is ~ 8 min. After the spectrum is recorded, the spatial distribution of the luminescence properties at the selected wavelength is mapped by raster scanning the sample. The luminescence map is formed by integrating the signal for each image pixel during 15 ms using a custom-built integrator and LabVIEW data-acquisition routine to collect and display the data.

The setup described above, in addition to absorption and photoluminescence mapping at a selected wavelength, also permits spatially resolved, high-resolution photoluminescence spectroscopy by zooming in on different features detected on

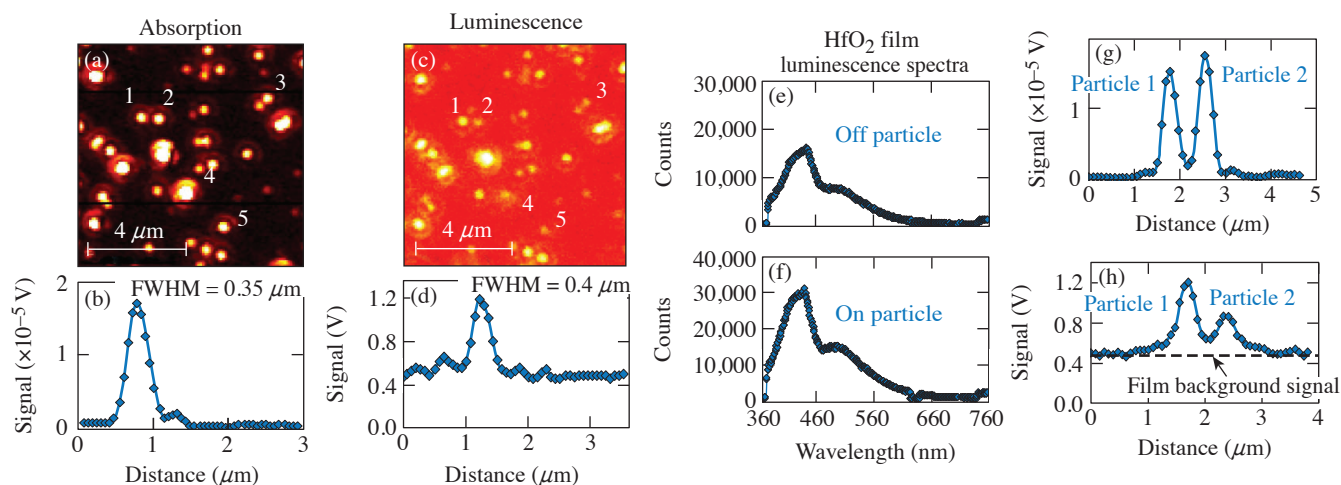
the absorption map. Also, using pulsed acousto-optic modulation of the pump beam, luminescence lifetimes as short as ~ 10 ns can be measured. Recently this setup was successfully used for the spectroscopic study of oxygen vacancies in hafnium oxide thin films.⁶

Examples of Absorption and Luminescence Mapping and Discussion

An important feature of the setup described above is the possibility to record absorption and luminescence maps at exactly the same location with submicrometer resolution. Figure 156.10 shows $10 \times 10\text{-}\mu\text{m}^2$ maps of 355-nm PHI absorption and 355-nm excited luminescence of $\sim 175\text{-nm}$ -thick HfO_2 thin film containing embedded Hf nanoparticles⁷ with sizes in the range from a few nm to 150 nm. Most of the particles detected on the absorption maps were also detected on the luminescence maps, although with much lower contrast (see Fig. 156.10). A typical cross section through the single-particle absorption image [see Fig. 156.10(b)] confirmed $\sim 0.35\text{-}\mu\text{m}$ FWHM (full width at half maximum) resolution generally defined by the intensity distribution in the focal spot of the pump and probe beams [see Eq. (1)]. In the case of luminescence, the resolution is defined by only the pump beam's focal-spot size. A typical cross section, revealing $\sim 0.4\text{-}\mu\text{m}$ resolution, is presented in Fig. 156.10(d). In both types of maps, one can find circular features surrounding each particle, which we attribute to an

Airy ring formed in the objective focal plane around the central spot of the pump beam, which also interacts with the particle.

The absorption map presented in Fig. 156.10(a) shows imaging of the nanoparticles with a high (up to 100) signal-to-background ratio [see Fig. 156.10(b)]. The luminescence map revealed a relatively strong homogeneous background signal, which reduced the contrast of the enhanced (up to $10\times$) signal at the Hf nanoparticle locations. The background signal comes from HfO_2 film luminescence, which was investigated in previous spatially resolved studies using near-ultraviolet (near-UV), 355-nm (Ref. 5) and UV, 266-nm laser excitation.⁸ The latter study demonstrated simultaneous mapping of 351-nm absorption, scattering, and 266-nm excited photoluminescence in HfO_2 film, although no direct correlation was found in the recorded maps. The spatial resolution in these maps was also relatively low, limited by the $30\text{-}\mu\text{m}$ diameter of the 351-nm pump beam. In the current work, the luminescence map [see Fig. 156.10(c)] was recorded at a 420-nm wavelength, corresponding to the maximum of the setup spectral sensitivity in the luminescence arm. Since the photoluminescence of spherical metal nanoparticles is typically very weak,⁹ we interpret observed signal enhancement at their location as a result of interaction of laser-excited free-electron oscillations (surface plasmon waves) inside the particle with the dipoles of electronic states responsible for photoluminescence in the host



G12478JR

Figure 156.10

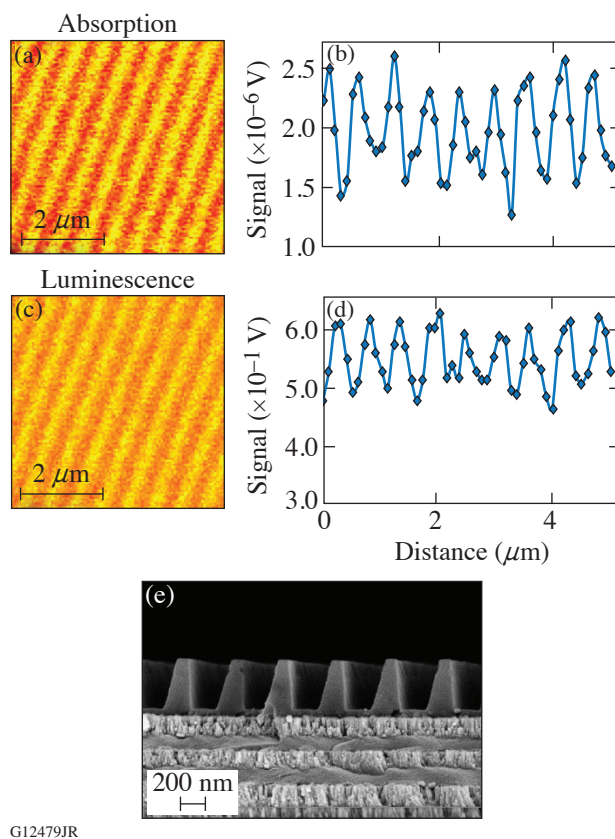
Absorption and photoluminescence mapping of the HfO_2 film with embedded Hf nanoparticles. [(a),(b)] $10\text{-}\mu\text{m} \times 10\text{-}\mu\text{m}$ PHI absorption map and corresponding signal cross section through one of the imaged particles; [(c),(d)] luminescence map of the same area and corresponding signal cross section through one of the imaged particles; [(e),(f)] luminescence spectra obtained by zooming on and off particle locations; [(g),(h)] cross sections through particles 1 and 2 on absorption and luminescence maps, respectively.

HfO₂ film. Considering that the 355-nm excitation wavelength lies far from the plasmon resonance for Hf nanoparticles, for which the maximum absorption is expected to be at wavelengths <200 nm (Ref. 10), the effect should not be large. The measurements confirmed that, on average, signal enhancement is $\sim 2\times$ at the particles' locations. This above interpretation is supported by comparing the spectra recorded at the sample locations free from particles and at the particles locations, which showed the same spectral profile [see Figs. 156.10(e) and 156.10(f)], with the only difference being the overall intensity. A similar but much stronger effect resulting from luminescence excitation directly into the gold plasmon peak was observed for gold nanoparticles deposited on AlGaIn with embedded Er³⁺ ions, where luminescence was excited by 532-nm laser light.¹¹ The theoretical description of such interaction can be found in Ref. 12.

A comparison of the two maps, absorption and luminescence depicted in Fig. 156.10, reveals that some particles showing a high absorption signal might exhibit very low luminescence enhancement [see particles designated by 2, 3, 4, and 5 in Figs. 156.10(a) and 156.10(c)]. A cross-sectional analysis [see Figs. 156.10(g) and 156.10(h)] of two particles (designated as 1 and 2 on the map), separated by only $\sim 1\ \mu\text{m}$, clearly shows that the strong absorption signal for particle 1 is replicated on the luminescence map, but for particle 2, with comparable absorption signal, luminescence enhancement is dramatically reduced. To find an explanation for this observation, we need to consider the main factors influencing signal formation in both cases. For embedded metal nanoparticles that are much smaller than the light wavelength, the PHI absorption signal depends strongly on the particle size and how efficiently the heat will be conducted to the surrounding matrix. In the porous coating material, the latter might cause some variations for particles whose size is comparable or smaller than the void size. In the case of luminescence, the enhancement caused by metal nanoparticles depends on particle size (existing optimum size for the enhancement¹²) may strongly vary with the distance from the closest oscillators, and may be reduced in the case of the few closely located particles because of not-in-phase oscillations.¹³ Taking all these factors into account, the luminescence signal in the vicinity of the particle might show a more drastic variation than the PHI absorption signal, which explains why the luminescence enhancement almost disappears at particle locations 2, 3, 4, and 5.

Another example of absorption and luminescence mapping with submicrometer resolution is presented in Figs. 156.11(a) and 156.11(c), which depict imaging of the dielectric grat-

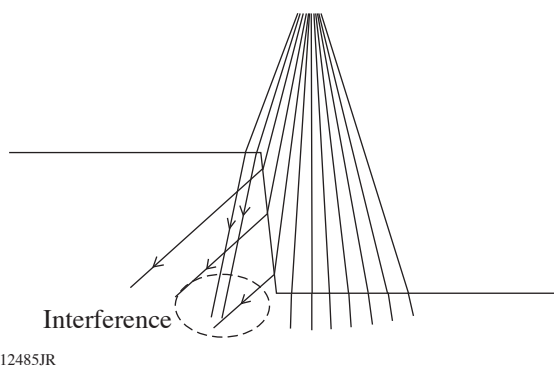
ing. The grating with 1740 grooves/mm is produced by a lithographic process applied to the top SiO₂ layer of multilayer dielectric coating deposited on a glass substrate, with HfO₂ and SiO₂ being high- and low-refractive-index materials, respectively.¹⁴ In this case, contribution to 355-nm absorption and luminescence also comes from HfO₂ layers, and the contrast is created because of periodic light-field enhancement resulting from interference effects caused by the grating profile (see Fig. 156.12). Ray-tracing analysis shows that these interference effects, for a beam focal spot comparable with a grating period, depend on the beam's lateral position, namely centering above the pillar or above the trench, and on the axial location of the focal spot. The latter was adjusted experimentally by fine tuning the axial position of the nanopositioning stage to obtain the highest contrast on the recorded images. A cross-sectional analysis [Figs. 156.11(b) and 156.11(d)] shows that the grating profile has a higher contrast $\nu = 0.56$ on absorption images,



G12479JR

Figure 156.11

Absorption and photoluminescence mapping of the multilayer dielectric grating. [(a),(b)] A $5\text{-}\mu\text{m} \times 5\text{-}\mu\text{m}$ PHI absorption map and corresponding signal cross section containing eight grating periods; [(c),(d)] a luminescence map of the same area and corresponding signal cross section through eight grating periods; (e) SEM image of the grating.



G12485JR

Figure 156.12
Schematic of the 355-nm ray tracing through the grating, illustrating possible interference effects in the material below the grating profile.

as compared to $\nu = 0.23$ on luminescence images, reduced mostly by a higher luminescence background signal, including electronic noise. The contrast ν was calculated using the following expression:

$$\nu = [I_{\max}(\text{avg}) - I_{\min}(\text{avg})] / I_{\min}(\text{avg}), \quad (2)$$

where $I_{\max}(\text{avg})$ and $I_{\min}(\text{avg})$ are the maximum and minimum signal values, respectively, averaged over several grating periods. The same analysis gave a grating period, averaged over eight cycles, of 567 nm, which is very close to the 575-nm period obtained from the 1740 grooves/mm specification and scanning electron microscope imaging depicted in Fig. 156.11(e).

Conclusions

To summarize, a versatile spectroscopic setup that permits the mapping of absorption and photoluminescence properties with submicrometer spatial resolution and high sensitivity has been described. The performance of the setup was illustrated by imaging Hf nanoparticles embedded in HfO₂ thin film and dielectric grating with a 575-nm period using both absorption and luminescence modes. Possible mechanisms contributing to contrast formation on acquired luminescence images include, in the case of Hf nanoparticles, the interaction of a particle's plasmon with local host oscillators, and in the case of grating imaging, interference effects. Further desirable improvements to the described setup would be to incorporate a wavelength-tunable pump source and implement new spectroscopic capabilities, like Raman scattering.

ACKNOWLEDGMENT

The author thanks H. Huang for performing ray tracing and B. Hoffman for providing SEM imaging of the dielectric grating.

This material is based upon work supported by the Department of Energy National Nuclear Security Administration under Award Number DE-NA0003856, the University of Rochester, and the New York State Energy Research and Development Authority.

REFERENCES

1. S. Berciaud *et al.*, Phys. Rev. B **73**, 045424 (2006).
2. S. Papernov, A. Tait, W. Bittle, A. W. Schmid, J. B. Oliver, and P. Kupinski, J. Appl. Phys. **109**, 113106 (2011).
3. M. Commandré and P. Roche, Appl. Opt. **35**, 5021 (1996).
4. A. Alexandrovski *et al.*, Proc. SPIE **7193**, 71930D (2009).
5. S. Papernov, A. A. Kozlov, J. B. Oliver, T. J. Kessler, A. Shvydkiy, and B. Marozas, Opt. Eng. **53**, 122504 (2014).
6. S. Papernov, M. D. Brunsman, J. B. Oliver, B. N. Hoffman, A. A. Kozlov, S. G. Demos, A. Shvydkiy, F. H. M. Cavalcante, L. Yang, C. S. Menoni, B. Roshanzadeh, S. T. P. Boyd, L. A. Emmert, and W. Rudolph, Opt. Express **26**, 17608 (2018).
7. S. Papernov, E. Shin, T. Murray, A. W. Schmid, and J. B. Oliver, Proc. SPIE **8530**, 85301H (2012).
8. A. Ciapponi *et al.*, J. Lumin. **129**, 1786 (2009).
9. S. Link and M. A. El-Sayed, Int. Rev. Phys. Chem. **19**, 409 (2000).
10. J. A. Creighton and D. G. Eadon, J. Chem. Soc. Faraday Trans. **87**, 3881 (1991).
11. M. T. Carlson, A. Khan, and H. H. Richardson, Nano Lett. **11**, 1061 (2011).
12. G. Sun, J. B. Khurgin, and R. A. Soref, Appl. Phys. Lett. **94**, 101103 (2009).
13. J. B. Khurgin, G. Sun, and R. A. Soref, Appl. Phys. Lett. **93**, 021120 (2008).
14. J. Keck, J. B. Oliver, T. J. Kessler, H. Huang, J. Barone, J. Hettrick, A. L. Rigatti, T. Hoover, K. L. Marshall, A. W. Schmid, A. Kozlov, and T. Z. Kosc, Proc. SPIE **5991**, 59911G (2005).